



**HAL**  
open science

## Mechanofluorochromic Material toward a Recoverable Microscale Force Sensor

Jan Patrick Calupitan, Arnaud Brosseau, Pierre Josse, Clément Cabanetos,  
Jean Roncali, Rémi Métivier, Clémence Allain

► **To cite this version:**

Jan Patrick Calupitan, Arnaud Brosseau, Pierre Josse, Clément Cabanetos, Jean Roncali, et al..  
Mechanofluorochromic Material toward a Recoverable Microscale Force Sensor. *Advanced Materials  
Interfaces*, 2022, 9, 10.1002/admi.202102246 . hal-03799181

**HAL Id: hal-03799181**

**<https://hal.science/hal-03799181v1>**

Submitted on 5 Oct 2022

**HAL** is a multi-disciplinary open access archive for the deposit and dissemination of scientific research documents, whether they are published or not. The documents may come from teaching and research institutions in France or abroad, or from public or private research centers.

L'archive ouverte pluridisciplinaire **HAL**, est destinée au dépôt et à la diffusion de documents scientifiques de niveau recherche, publiés ou non, émanant des établissements d'enseignement et de recherche français ou étrangers, des laboratoires publics ou privés.

# Mechanofluorochromic Material toward a Recoverable Microscale Force Sensor

Jan Patrick Calupitan, Arnaud Brosseau, Pierre Josse, Clément Cabanetos, Jean Roncali, Rémi Métivier,\* and Clémence Allain\*

Among the multiple classes of mechanofluorochromic (MFC) compounds reported in recent years, simple donor–acceptor molecules involving oligoxyethylene *N*-substituted diphenylamine connected to a dicyanovinyl group by a thienyl spacer constitute a specific class of mechano-stimulable smart materials with a unique combination of properties including turn-on mechanofluorochromism with red-light photoluminescence emission, turn-off second harmonic generation, and self-recovery in ambient conditions. While the dynamics of the MFC processes of thin films of these materials have already been investigated, the correlation of the behavior observed at the macroscale with elemental processes taking place at the micro- and nanoscopic scales remains largely unexplored. In this work, atomic force microscopy (AFM) coupled with wide-field and confocal optical microscopies is used to investigate the turn-on/recovery MFC behavior of microcrystals and nanostructures. It is shown that the red light photoluminescence of microcrystals and nano-objects can be turned-on by contact AFM and that the intensity of light emission is linearly correlated to the applied nominal force. Recovery is associated with a decrease in emission intensity, which can be reactivated again by subsequent contact scans. These results thus pave the way toward the development of micro-/nanoscale recoverable force-sensing technologies based on this particular class of smart molecular materials.

## 1. Introduction

Stimuli responsive materials<sup>[1]</sup> constitute functional building blocks of next generation devices: a wide variety of new technologies, ranging from sensors<sup>[2–6]</sup> to molecular electronics<sup>[7–11]</sup> and multilevel security devices,<sup>[12]</sup> rely on changes in optical properties upon application of stimuli. Light,<sup>[7–11]</sup> heat,<sup>[10,13–15]</sup> solvent (and its vapor),<sup>[16–18]</sup> and mechanical forces,<sup>[2,6,19–22]</sup> modify the structure of materials at the (supra)molecular level to effect changes in both absorption and emission properties. Among these stimuli-responsive processes, mechanofluorochromism,<sup>[20–50]</sup> the change

in optical properties upon application of mechanical stimuli such as scratching or grinding, promises applications for force sensors.<sup>[20–36]</sup> Emission changes of coordination complex crystals,<sup>[24]</sup> polymeric microcrystals,<sup>[30]</sup> and organic fluorophores,<sup>[31–36]</sup> have been correlated to an applied force or pressure for new anticounterfeiting technologies<sup>[23–28]</sup> and biological stress probes.<sup>[29]</sup>

Force sensing via mechanofluorochromic activity has been reported at the micro/nanoscales by direct measurement of emission changes upon in situ application of varying amounts of mechanical stimulus.<sup>[24,30,31,33–36]</sup> Yet, one issue that remains to be explored is the recovery of the material. Emission changes, correlated with applied force, are induced by morphological changes in the material.<sup>[20–50]</sup> This means that subsequent sensing events, after the initial application of force, necessitate recovering the original morphology—a process not so straightforward as this usually requires thermal annealing,<sup>[38]</sup> solvent fuming,<sup>[25,27]</sup> or recrystallization.<sup>[20–22,37]</sup>

Self-recovery, the spontaneous return to the initial state (of absorption, emission and morphology) of the scratched/ground material under ambient conditions, has been observed in derivatives based on Au(I) complexes,<sup>[28]</sup> pyrene,<sup>[39,40]</sup> anthracene,<sup>[41,42]</sup> tetraphenylethene,<sup>[43,44]</sup> indolylbenzothiadiazole,<sup>[45]</sup> triphenylamine,<sup>[46]</sup> boron-coordinated  $\beta$ -diketonate complexes,<sup>[47]</sup> and hexathiobenzene.<sup>[48]</sup> However, many MFC-active materials are left unexplored for multiple-use force sensing applications, not only due to the complexity of instrumentation required for such studies,<sup>[24,30,31,33–36]</sup> but also due to the lack of molecular design leading to reversibility<sup>[40]</sup> and a clear understanding of mechanism of self-recovery.<sup>[30,45]</sup>

J. P. Calupitan, A. Brosseau, R. Métivier, C. Allain  
Université Paris-Saclay, ENS Paris-Saclay  
CNRS, PPSM, Gif-sur-Yvette 91190, France  
E-mail: remi.metivier@ens-paris-saclay.fr;  
clemence.allain@ens-paris-saclay.fr

P. Josse, C. Cabanetos  
Moltech-Anjou  
CNRS UMR 6200  
University of Angers  
Angers 49045, France

J. Roncali  
Supramolecular Organic and Organometallic Chemistry Center  
Babes-Bolyai University  
11 Arany Janos str., Cluj-Napoca 400028, Romania

 The ORCID identification number(s) for the author(s) of this article can be found under <https://doi.org/10.1002/admi.202102246>.

© 2022 The Authors. Advanced Materials Interfaces published by Wiley-VCH GmbH. This is an open access article under the terms of the Creative Commons Attribution-NonCommercial-NoDerivs License, which permits use and distribution in any medium, provided the original work is properly cited, the use is non-commercial and no modifications or adaptations are made.

DOI: 10.1002/admi.202102246

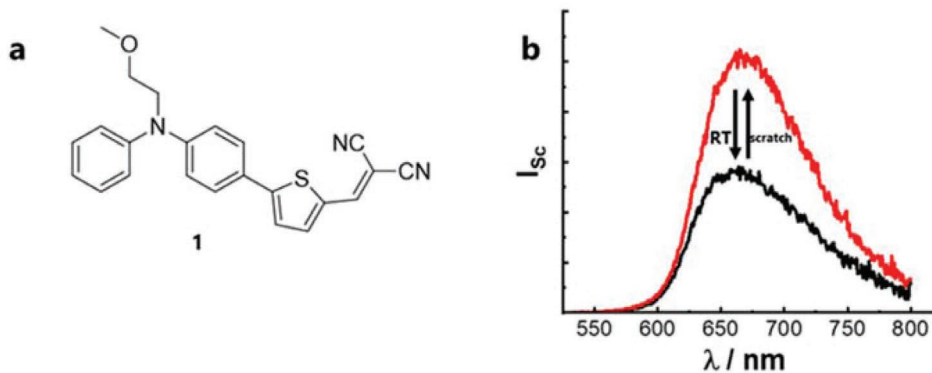


**Figure 1.** a) Structure of **1** from which films were fabricated. b) Mechanofluorochromic behavior of films. Scratching caused a reversible redshift and increase in emission of the films ( $\lambda_{\text{exc}} = 400 \text{ nm}$ ).

Recently, mechanofluorochromic films based on a family of diphenylamine compounds functionalized with  $\pi$ -extended thiophene and dicyanovinyl groups and N-substituted with oligo-oxyethylene groups were developed.<sup>[23,50]</sup> Freshly prepared red films emitted red light and spontaneously evolved to clear films with partly quenched emission. Mechanical scratching, heating, or solvent fuming of clear films reactivated their red color and emission.<sup>[23,50]</sup> Then, activated red films spontaneously recovered the clear state again without external stimulation at room temperature. This self-recovering step was associated with the formation of H-type aggregates with  $\pi$ -stacked aromatic rings that typically display aggregation-caused quenching of emission.<sup>[23,50]</sup> Furthermore, the length of oligo-oxyethylene chain was found to modulate the kinetics of recovery and molecular packing structure of the material.<sup>[50]</sup> These compounds provide another example of strongly dipolar chromophores, containing pendant electronically inert groups, having electronic properties invariant in solution but pack to drastically different motifs in the solid state, leading to distinct electronic and optical properties.<sup>[51,52]</sup>

This self-recovering mechanofluorochromic activity led us to explore the material as a multiple-use force sensor. We chose to focus on the mechanofluorochromism of the compound 2-((5-(4-((2-methoxyethyl)(phenyl)amino)phenyl)thiophen-2-yl)methylene)malononitrile (**1**, **Figure 1a**) for practical reasons. The auto-recovering step (from red to clear) of films fabricated from this compound was indeed shown to be in the scale of  $\approx 10 \text{ h}$ ,<sup>[50]</sup> i.e., longer than our experimental timescales, allowing us to characterize the films despite their dynamic nature. Due to the suspected polymorphic nature of the films,<sup>[50]</sup> we decided to perform microscopy experiments to identify the morphology of the micro/nanostructures responsible for mechanofluorochromism. Therefore, we investigated the mechanofluorochromism of the material at the microscale with two aims: 1) from a basic point of view, to trace the macroscale behavior to properties of the micro/nanostructures and; 2) from a technological point of view, to demonstrate a proof-of-concept for this material as a microscale multiple-use force sensor.

In this paper, we first present the macroscale mechanofluorochromic activity of the films before delving into the microscale by a coupled fluorescence and atomic force microscopy (AFM) study. The fluorescence microscope with wide-field and confocal

modes allowed to interrogate changes in emission properties of the films at the microscale upon mechanical stimulation. The AFM served not only to probe the topography of the films (via tapping mode scans) at the microscale, but also as minute mechanical stimulation (via contact mode scans). We attempt to characterize the emitting species responsible for the mechanofluorochromic activity. Once this is established with a constant nominal force, we show that the response of the material varies with changing vertical nominal force applied. With this, we demonstrate in the last part that the mechanofluorochromic behavior of the material can lead to a recoverable microscale force sensor.

## 2. Results and Discussion

### 2.1. Macroscale Mechanofluorochromism

The synthesis of **1** was previously reported.<sup>[50]</sup> In this section, we recall some of its previously reported properties<sup>[50]</sup> and present additional data relevant to the current study. Solutions of **1** in tetrahydrofuran (THF) showed a red color ( $\lambda_{\text{max}} = 490 \text{ nm}$  or  $2.54 \text{ eV}$ ) and emitted in the red region of the visible spectrum centered at  $620 \text{ nm}$  ( $2.00 \text{ eV}$ ) with a quantum yield of 0.06 (Figure S1, Supporting Information). Time-dependent density functional theory calculations reproduced these transitions in absorption and emission: calculated absorption energy =  $2.44 \text{ eV}$  (4% error vs experimental  $\lambda_{\text{max}}$ ); calculated emission energy =  $2.25 \text{ eV}$  (13% error). Calculations further showed that the  $S_0 \rightarrow S_1$  absorption is a purely HOMO-LUMO transition. HOMO and LUMO maps (Figure S2, Supporting Information) showed the reported charge-transfer character of the compound.<sup>[50]</sup>

Drop-deposition of solutions of **1** in THF resulted in red films. This spontaneously evolved to a clear color after 14 hours at room temperature.<sup>[50]</sup> The emission maximum of the red films shifted to the red ( $\lambda_{\text{max,em}} = 670 \text{ nm}$ ) with a lower quantum yield ( $\Phi = 0.048 \pm 0.002$ ) relative to the solution state. Upon evolution, the emission of the clear films was slightly quenched ( $\Phi = 0.035 \pm 0.003$ ) accompanied by a slight blue-shift of emission ( $\lambda_{\text{max,em}} = 660 \text{ nm}$ ) (Figure 1b). Mechanical stimulation via scratching reactivated the red color and brighter redshifted emission of the films. Thermal annealing and solvent fuming were also found to effect the activation of

the red state. Then, in a self-recovering manner, the resulting red film returned to its clear state again without application of any external stimuli.

From the solution state to the red and clear states of the material, the slight decrease in emission quantum yield indicated aggregation induced quenching. This was also observed in suspensions of the compound in THF-water systems.<sup>[50]</sup> In typical triphenylamine derivatives, three phenyl rings twist around the N atom due to steric hindrance, preventing the formation of aromatic  $\pi$ - $\pi$  interactions so that emission enhances upon aggregation.<sup>[22,38,54]</sup> The two phenyl rings and one methoxyethyl chain in **1** did not present enough steric hindrance around the N atom to prevent  $\pi$ - $\pi$  stacking interactions, leading to the observed extent of emission quenching.

Based on powder X-ray diffraction (PXRD) measurements, the evolution from the red to the clear state was attributed to some solid-state ordering, or even recrystallization, involving the formation of H-aggregates directed by stacking and H-bonding interactions.<sup>[50]</sup> The clear films displayed sharp diffraction patterns that match those predicted from the single-crystal structure, indicating that the former adopts a globally similar arrangement (head-to-tail) as the latter. Scratching the clear films decreased the intensity of diffraction peaks, indicative of a disruption of this supramolecular structure.<sup>[50]</sup> These results showed that the mechanofluorochromic behavior from the less emissive clear state to the more emissive red state is due to a transition from an ordered structure, probably crystalline, to an amorphous one. Meanwhile, the self-recovering step (spontaneous evolution of the red films to the clear state) is ascribed to a degree of solid-state ordering such as recrystallization.

We note that the clear state may not be completely crystalline, nor the red state completely amorphous. The presence of polymeric structures in these films was previously suspected.<sup>[23,50]</sup>

The clear state may present incomplete ordering or partial recrystallization only while the red state may still contain ordered structures (as scratching may not fully disrupt the organization of structures). We therefore investigated the films via microscopy to further delve into the emission properties at the microscale associated with local and quantitative mechanical stimulation.

## 2.2. Microscale Mechanofluorochromism: AFM×Wide-Field Microscopy

Microscopy samples were fabricated by drop-depositing solutions of **1** (0.5–1.0 mg mL<sup>-1</sup> in THF) on previously cleaned glass slides. The resulting red films were dried and allowed to evolve to the clear state at room temperature overnight. Experiments involved an AFM installed on an inverted wide-field optical microscope. This allowed us to simultaneously probe the topography and emission of distinct objects on the sample (see experimental details) The AFM tip also served for local stimulation of the material via contact-mode scans.

Imaging revealed the polymorphic nature of the film: we observed a) crystals with dimensions of a few microns (Figure 2) and b) rod-like nanostructures (Figure 3). Any preparation resulted in both structures but the latter was favored when solvent evaporation was accelerated by drying the samples under vacuum.

Figure 2a shows microcrystals (blue arrows) with darker inner parts and emissive edges typical of waveguiding effects previously observed in microcrystals of transition metal complexes<sup>[37]</sup> and organic fluorophores.<sup>[49]</sup> (See Figure S3, Supporting Information, for other sample images.) AFM topography images (Figure 2b) show the flat surface of the crystals,

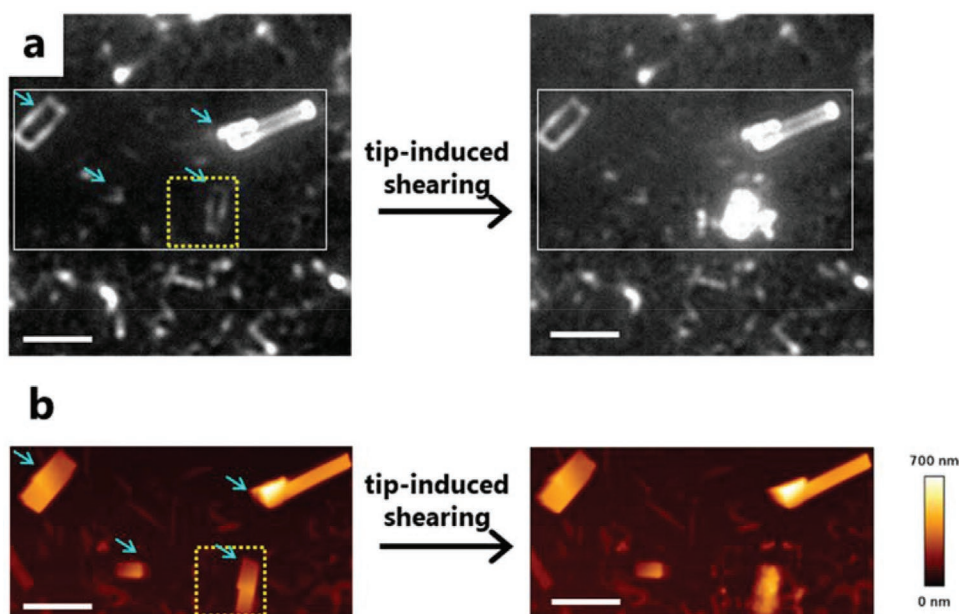


**Figure 2.** a) Wide-field fluorescence images of microcrystals before and after contact-mode scans by the AFM tip (vertical nominal force 100 nN and tip velocity 1  $\mu\text{m s}^{-1}$ ) show a localized increase in fluorescence signal on the stimulated area marked by a dotted yellow square. Cyan arrows point to microcrystals. White box shows the area probed by AFM topography scans on (b). Scale bar = 5  $\mu\text{m}$ .  $\lambda_{\text{exc}}$  = 480 nm.

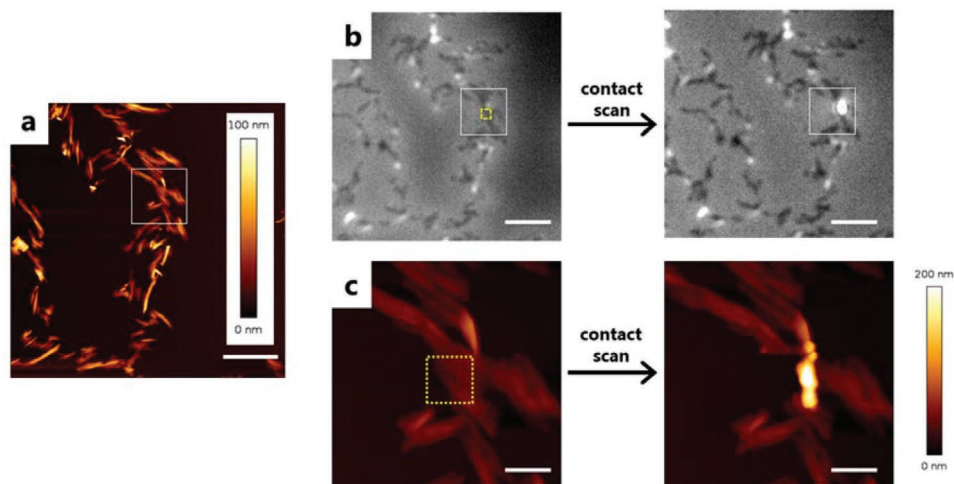


**Figure 3.** a) Large scale AFM topography image of nanothreads before contact mode scratching. Scale bar = 5  $\mu\text{m}$ . b) Corresponding wide-field fluorescence images of nanothreads before and after contact-mode scan by AFM tip (on the dotted yellow region, 100 nN, tip velocity 1  $\mu\text{m s}^{-1}$ ) show localized increase in emission intensity on the stimulated area. Scale bar = 5  $\mu\text{m}$ .  $\lambda_{\text{exc}} = 480 \text{ nm}$ . Solid white box shows the area zoomed in on (c). c) AFM images show changes in morphology before and after contact mode scan on the dotted yellow area. Scale bar = 1  $\mu\text{m}$ .

as confirmed by the phase images (Figure S4, Supporting Information). Among the  $\approx 50$  crystals observed, most were rectangular while some had a parallelepiped shape. They vary widely in size with lengths  $6.6 \pm 4.2 \mu\text{m}$ , widths  $2.1 \pm 0.7 \mu\text{m}$  and, heights  $270 \pm 90 \text{ nm}$ .

To check the mechanofluorochromic properties, we applied mechanical shearing stress by setting the AFM to scan in contact mode on an area containing a crystal. (Figure 2a,b, dotted yellow square, vertical nominal force 100 nN, tip velocity 1  $\mu\text{m s}^{-1}$ .) Subsequent fluorescence imaging revealed a dramatic emission increase localized on the crystal and on the periphery of the sheared region. (Figure 2a, see Figure S5, Supporting Information, for difference image.) The contact scan displaced some material onto the sides of the stimulated region but a simple accumulation of material could not explain the brighter signals, localized on the crystal itself. AFM topography images (Figure 2b) showed disruption of the flat surface while phase images revealed the heterogeneity of the crystal poststimulation (Figure S4, Supporting Information). Therefore, the brighter emission upon the contact scan is a true OFF-ON mechanofluorochromic response—due to morphological changes—not just an accumulation of emissive material.

In other regions of the sample, AFM topography imaging (Figure 3a) showed nanostructures having heights less than 100 nm. These structures are less emissive than the microcrystals (sometimes even darker than the sample background) and are dotted with bright emissive spots (Figure 3b, Figure S6, Supporting Information, for other sample crystals). On wide-field optical images, they extend over several micrometers in different directions but high-resolution AFM images (Figure 3a,c) show shorter and thinner structures having dimensions  $2.3 \pm 0.7 \mu\text{m}$  in length,  $480 \pm 150 \text{ nm}$  in width, and  $40 \pm 20 \text{ nm}$  in height (averaged over  $\approx 20$  sample structures).

We likewise checked the mechanofluorochromic activity of the nanostructures by performing contact mode scans on the region marked by a dotted yellow square on Figure 3b,c (Vertical nominal force 100 nN, tip velocity 1  $\mu\text{m s}^{-1}$ ). This resulted

in immense increase of fluorescence signal localized on the stimulated area (Figure 3b; see Figure S7, Supporting Information, for difference image). AFM topography images showed displacement of material onto the sides of the area scanned (Figure 3c). Phase images confirmed that this accumulated material does not present a homogenous structure distinctive of the nanostructures prestimulation (Figure S8, Supporting Information). The strong emission coincides with AFM tip-induced morphological changes similar to the mechanofluorochromic response of microcrystals. These observations are clarified in more detail in the next section.

To sum up the AFM and wide-field fluorescence microscopy experiments, we uncovered at least three morphologies on the clear films: 1) microcrystals with bright edges; 2) dark nanostructures; and 3) and disordered bright spots randomly scattered around them. The strong emission and disorder of the bright spots indicate that they may be equivalent to the amorphous emissive red films in the macroscale. Both microcrystals and nanostructures presented homogenous morphologies susceptible to disruption when mechanical stress is applied by the AFM tip. Further, in both cases, mere approach of the tip, even with application of higher setpoints up to  $\approx 300 \text{ nN}$ , did not cause localized recovery of emission. The shearing force from the lateral motion of the rigid tip was necessary to induce changes in emission, unlike in previous studies where increasing emission signals were observed upon application of compressive stress.<sup>[33]</sup>

### 2.3. Microscale Mechanofluorochromism: AFM $\times$ Confocal Mode

To gain insights into the mechanofluorochromism at the sub-micron scale, we set the fluorescence microscope in confocal mode, allowing the measurement of local spectral signature with a spectrograph. (See Experimental Details and Figure S9, Supporting Information, for the workflow of a typical experiment.)

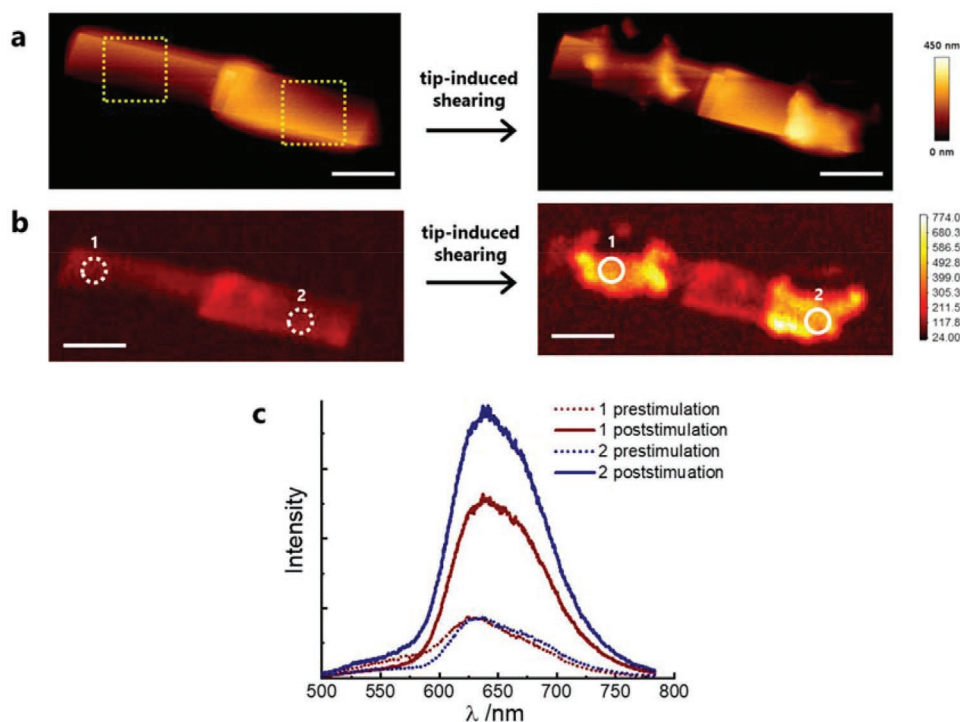


**Figure 4.** a) AFM topography images before and after AFM contact scans ( $100\text{ nN}$ ,  $1\ \mu\text{m s}^{-1}$ ) show disruption of the crystalline structure upon stimulation. b) Fluorescence confocal images, that correspond well to the topography images, show increase in emission signal poststimulation. White circles on (b) show where c) emission spectra were collected. Dotted circles for prestimulation spectra, solid circles for poststimulation. c) Emission spectra show the increase in fluorescence and slight redshift of maximum poststimulation. Dotted lines for prestimulated crystals and solid lines for poststimulation. Scale bar =  $2\ \mu\text{m}$ ,  $\lambda_{\text{exc}} = 445\text{ nm}$ .

High resolution AFM showed the flat topography of an isolated microcrystal composed of two domains (Figure 4a). We performed two contact scans localized on the surface of the crystal (marked by the dotted yellow squares on Figure 4a,  $100\text{ nN}$  vertical nominal force,  $1\ \mu\text{m s}^{-1}$  tip velocity) in order to apply well-defined mechanical stress on the crystal. This time, we managed to disrupt the local morphology of the crystal itself, taking care to keep other regions intact, as opposed to Section 2.2 in which the whole piece of the crystal was affected. Line profiles show localized damage on the areas scanned; untouched areas remained the same (Figure S10, Supporting Information). Confocal fluorescence imaging (Figure 4b) showed 2 to 3 times higher emission signals of the stimulated areas while areas untouched remained the same. (See Figure S11, Supporting Information, for difference image.)

Higher emission intensities were measured not only where material accumulated poststimulation but also on regions where no increase in topography was observed. (Figure S10, Supporting Information, shows the comparison of line profiles of topography and confocal images pre- and poststimulation.) This means that the increase in emission intensity was not caused by accumulation of material but due to transitions in morphology of the microcrystal upon stimulation. This confirms results of Section 2.2: a local transition from crystalline to amorphous states under mechanical stress accompanied a dramatic increase of emission signal.

We also measured emission spectra before and after mechanical stimulation by the AFM tip. The microcrystals initially emitted in the red with maximum at  $630\text{--}640\text{ nm}$ . Upon AFM-tip stimulation, the spectra not only increased in intensity but shifted to the red by  $10\text{--}20\text{ nm}$  as well (Figure 4c; see Figure S12a, Supporting Information, for normalized spectra). Meanwhile, areas untouched did not show changes in emission spectra (Figure S12b, Supporting Information). These observations mirror the mechanofluorochromic behavior of the clear films at the macroscale: mechanical stimulation caused both an increase and redshift of emission.

For the nanostructures, AFM-tip stimulation of two  $1\ \mu\text{m} \times 1\ \mu\text{m}$  areas (dotted yellow squares) on Figure 5a ( $100\text{ nN}$ ,  $1\ \mu\text{m s}^{-1}$ ) disrupted the thread-like morphology. Confocal images before and after stimulation confirmed changes in topography as probed by the AFM. Figure 5b also shows the increase in emission intensity localized on the accumulated material. In both stimulation events depicted, material accumulates at the periphery of the sheared region. This usually happens on the lateral scanning directions (left or right sides) or on the top of the region. In both shearing events, some material accumulated on top, lower left, and to right side of the scratched region, (Figure 5a, yellow dotted square) which all display relatively higher emission signals than the unstimulated areas.

Under confocal microscopy, these nanostructures exhibited similar emission spectrum changes as the microcrystals. (Figure 5c) Before mechanical stress via the AFM tip,

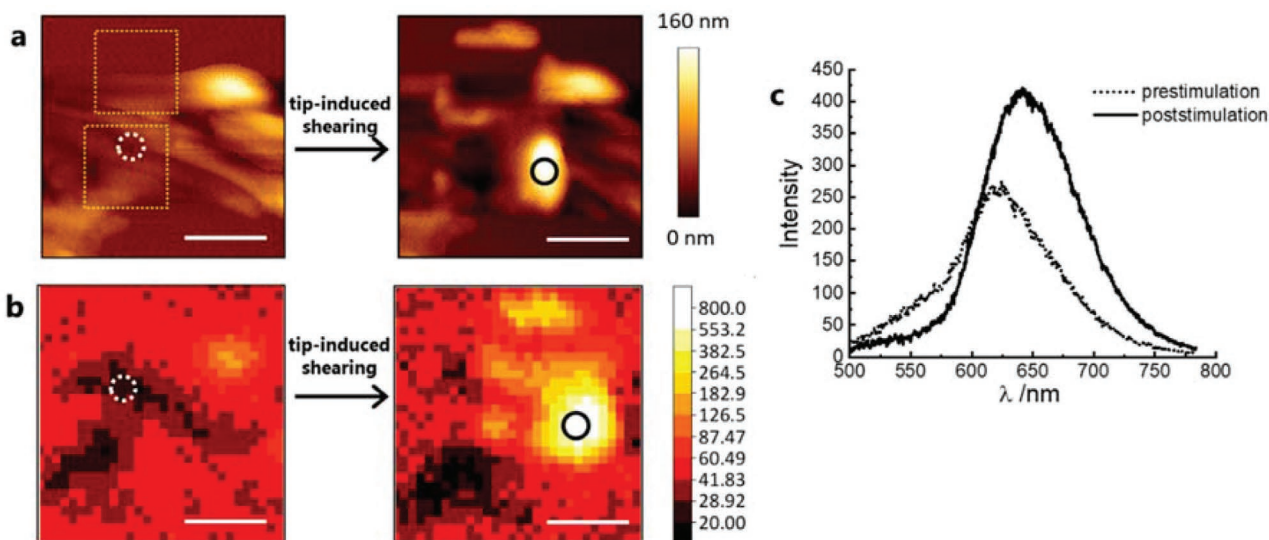


**Figure 5.** a) AFM topography images show morphology changes before and after stimulation via AFM contact mode. Yellow dotted squares show the region scanned (vertical nominal force 100 nN). b) Fluorescence confocal images before and after stimulation showing increase of fluorescence. In both (a) and (b), the white dotted circle and the black solid circle indicate the regions where emission spectra were collected before and after stimulation respectively, shown on (c). All scale bars correspond to 1  $\mu\text{m}$  scale. Note a slight shift between the AFM and confocal images. The circles may serve to mark this shift, as they mark the same areas pre- and postshearing.  $\lambda_{\text{exc}} = 445$  nm.

we measured weak emission centered at 630 nm on the area enclosed by the dotted white circle on Figure 5b. The contact scans displaced some amount of material to the right of the scanned region, which displayed a  $\approx 10$  nm redshift and stronger emission (black solid circle, Figure 5b). We note that these changes in emission spectra and intensity are independent of where the material accumulated postshearing. More importantly, changes in spectral profile upon mechanical stimulation discount the possibility that the brighter emission was due to a simple accumulation of material (since this would just result in the same spectral shape) but to morphological changes at the supramolecular level, i.e., from an ordered, probably even crystalline, to amorphous states. Lastly, we note that spectra in areas without mechanical stimulation showed no significant changes in emission spectral profile.

Complete sets of experiments, which include AFM topography imaging, confocal imaging, and spectral measurements before and after tip-induced mechanical stress, were repeated several times on other isolated microcrystals and other regions containing nanostructures, producing consistent results. Figure S14 and S15 (Supporting Information) show other typical examples of localized stimulation on a microcrystal and nanostructures respectively.

#### 2.4. Microcrystals toward a Reversible Local Force Sensor

These results indicate that the macroscale behavior of the clear films resulted from the microscale mechanofluorochromic properties of both microcrystals and nanostructures. Mechanical stimulation caused an increase and redshift in fluorescence signal in both structures. PXRD<sup>[50]</sup> showed that this was due to disappearance of crystalline structures upon macroscopic grinding; microscopy experiments demonstrated the

local disruption of ordered structures upon AFM-tip induced shearing. Differences in emission spectral positions between the macroscale clear films ( $\lambda_{\text{max}} \approx 660$  nm) and the microscale objects (microcrystals at  $\approx 620$ – $630$  nm, nanostructures at  $\approx 630$  nm) could be attributed to the nonhomogeneity and thickness of the former. We also note the differences in the range of emission intensities of microcrystals and nanostructures: microcrystals have emission intensities at least 5–10 times higher than the nanostructures. Even if microcrystals and nanostructures have similar mechanofluorochromic behavior, they probably display polymorphic supramolecular structures.

For practical reasons, we chose to test microcrystals for force sensing since the more pronounced displacement of material on nanostructures may prevent quantitative experiments. We tested the correlation between fluorescence increase and applied force as measured by the nominal setpoint of the AFM tip during contact scans. A  $1 \mu\text{m} \times 1 \mu\text{m}$  region was chosen on a crystal extending longer than  $10 \mu\text{m}$  and a constant tip velocity of  $1 \mu\text{m s}^{-1}$  was applied for the AFM contact scans of varying forces. Applying vertical forces ranging from 50 to 150 nN did result in varying increases in fluorescence (Figure 6a,b). The fluorescence recovery was calculated as the difference between the emission signal of the stimulated region before and after the contact scan. Between 50 and 70 nN, we measured a constant level of recovery. Increasing from 70 to 120 nN resulted in a linear increase in fluorescence recovery ( $R^2 = 0.983$ ). Above 120 nN, no further increase in fluorescence recovery was observed. (Figure 6a)

In another experiment, we performed the same series of contact-mode scans on another crystal and the same dependence between fluorescence recovery and force was observed (Figure S16, Supporting Information). The correlation was likewise linear ( $R^2 = 0.865$ ) on the same range of 70–120 nN while no further evolution was observed below and above this

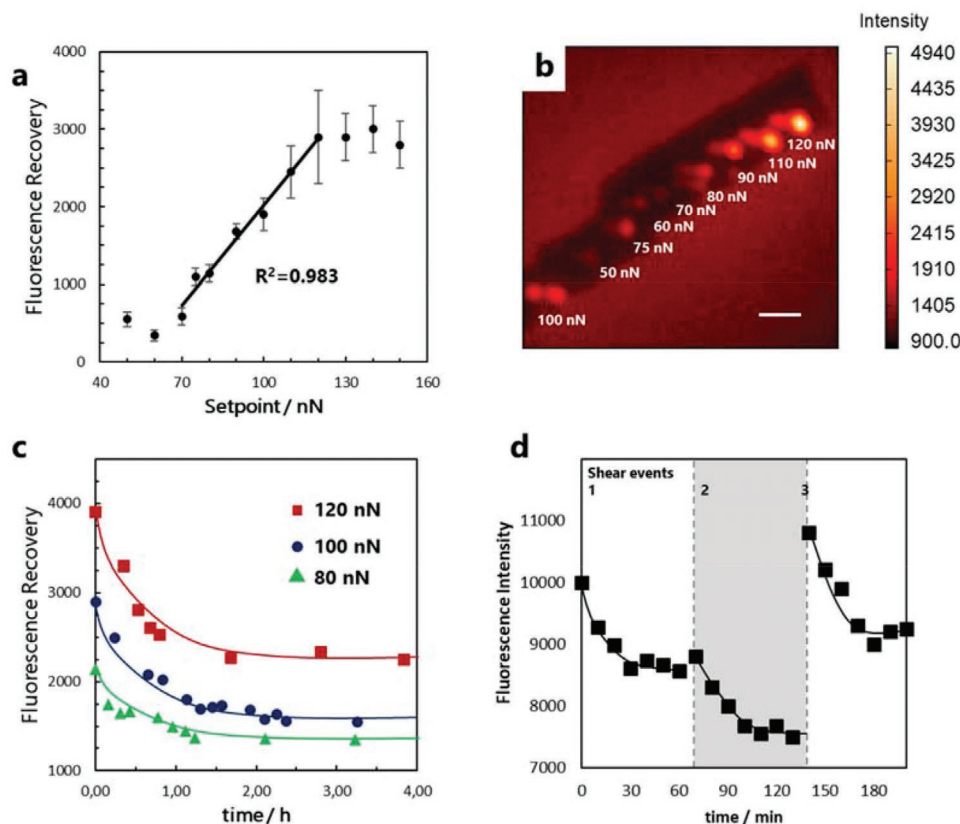


**Figure 6.** a) Dependence of fluorescence recovery (difference in emission signal before and after contact scans) of the stimulated area regions versus vertical nominal force. b) Wide-field fluorescence image of microcrystal stimulated with varying nominal force. Scale bar = 2  $\mu\text{m}$ . c) Evolution of fluorescence signal poststimulation. d) Evolution of signal poststimulation followed by two more cycles of stimulation. For (c) and (d), lines are drawn as guide to the eye only.

range. Three response regimes were observed in both cases: (1) a finite range of forces in which a linear response was observed; (2) below this range in which the emission recovered did not vary with force; and (3) above this range in which saturation was observed. In the linear response regime, the direct correlation between emission changes and applied nominal force corresponds to a linear extent of morphological disruption of the material upon scratching. The higher emission signals must be due to higher amounts of accumulated material upon shearing. Below this regime, the nominal force applied did not significantly depend on the nominal force applied. Above the linear regime, the higher forces did displace more material (as can be seen on Figure S19, Supporting Information, vs Figure 6b) but after a certain amount/height of material displaced, the emission signal did not increase further; the material seemed to stack over the localized area so the emitting species at the bottom of the accumulated material would be covered by others. Any additional material concentrated over a localized point would not contribute to the emission signal.

We recall that although we observed varying emission recoveries by changing the vertical nominal force (contact mode setpoint), the material is responsive to lateral shearing force and not compressive stress applied vertically. Figure 6a invokes an indirect correlation since the lateral shearing force (also

referred to as friction force) is directly proportional to the vertical normal force (setpoint) by the friction coefficient  $\mu$ :  $F_{\text{lateral}} = \mu F_{\text{normal}}$ .<sup>[35]</sup> However, given the technical difficulties involving calibration and tip variabilities regarding lateral force measurements,<sup>[35,53]</sup> with articles demonstrating such only recently,<sup>[35]</sup> we chose to simply report the emission recovery dependence versus the vertical nominal force (setpoint) instead of  $F_{\text{lateral}}$ .

To check whether the spontaneous return of the scratched red films in the macroscale to the clear state could be observed at the microscale, we followed the evolution of fluorescence intensity collected under the microscope for several hours on each of the spots on Figure 6b. Figure 6c plots the emission signal as a function of time poststimulation for the spots corresponding to 120 nN, 100 nN, and 80 nN. (See Figure S17, Supporting Information, for the other forces.) Within 1–2 h, fluorescence signal decreased to a level between 50–70% of the initial recovered fluorescence. Beyond this time scale, no significant changes in emission signal were observed. In another experiment, the evolution of emission signal after poststimulation was followed 3–5 d poststimulation and no more changes were detected (Figure S18, Supporting Information).

In all cases, we did not observe a complete return to the original emission of pristine microcrystals. AFM imaging did not show morphological changes poststimulation (Figure S19, Supporting Information). Nevertheless, the decrease in



fluorescence signal was sufficient to deduce rearrangement of molecules at the supramolecular level, even in the solid state. This fluorescence quenching could be interpreted as a self-recovering step from the highly emissive (amorphous) phase to the less emissive (ordered) structures.

We therefore attempted multiple AFM-tip shearing events over the same area, each followed by 1-hour recovery time in between. Three shearing events were performed (Figure 6d). With each shearing, emission intensity significantly increased and then spontaneously decreased after 30 min. These results illustrate that the microcrystals display a similar recovery behavior as films at the macroscale: subsequent spontaneous recovery followed scratching cycles. We note differences in the recovered signal upon each shearing event due to possible tip contamination. Although we checked whether the tip could deposit material onto an empty spot (Figure S20, Supporting Information), we could not exclude this possibility over multiple shearing events over the material. In addition, the localized nature of the measurements (and shearing) makes the experiments technically delicate: ideally, the stimulation should be performed on exactly the same area, otherwise, discrepancies due to local differences in the amount of the material and accumulation might cause slight deviations in the recovered signal. Nevertheless, these results show a proof-of-concept for a quantitative multiple-use force sensor at the microscale without thermal annealing.

### 3. Conclusion

Using a coupled AFM and optical microscope, we have linked the reversible macroscale mechanofluorochromic behavior of films of an organic luminescent compound to the microscale behavior of microcrystals and nanostructures. Microscopy demonstrated that the disruption of ordered and weakly emissive structures led to a redshifted highly emissive amorphous phase. This emissive phase could also spontaneously return to the less-emissive state at the microscale. Lastly, fluorescence enhancement upon stimulation correlated well with varying minute forces as low as 50 nN, with linear quantification from 70–120 nN. These results present a proof-of-concept demonstration of the material as a recoverable force sensor at the microscale.

Theoretically, resolution corresponding to the thickness (and morphology) of the tip could be achieved, with detection limits governed by the brightness of the emitting material. We note that although we attempted to vary the force applied on the material by changing a nominal setpoint applied vertically, the material is responsive to shearing forces applied laterally since emission changes (both increase upon shearing and decrease upon healing) are mostly visible on the displaced material. No emission changes were observed when the tip was simply approached on the sample, even with higher setpoints. In addition, for a real-world force sensor, the system must be adapted to all types of forces. The current study complements other studies that correlate emission changes due to varying compressive<sup>[24,33]</sup> forces. To advance this material toward a real-world force sensor, it would be necessary to investigate, and eventually control, the formation of the nanothreads/microcrystals. This would lead to microcrystals of reproducible

sizes, emission properties, and fluorescence increase upon mechanical stress. The influence of the type of force, such as scratching, shearing, or compression, may be studied as well using different geometries and stiffness of tips. The effect of different AFM contact mode scan parameters other than the setpoint such as scanning speed, scanning direction, and other tip parameters (force constant, sensitivity, etc.) should be tested as well. This could be standardized by directly measuring lateral shearing force from contact mode scans, which was demonstrated recently by friction force microscopy.<sup>[35]</sup>

Mechanofluorochromic materials have been greatly studied at the macroscale. How (supra)molecular structures and interactions relate to changes in photophysical properties and morphologies have been widely elucidated.<sup>[20–22]</sup> With interest from both basic and technological perspectives, these experiments on mechanofluorochromism can be pushed down to the micro- and nanoscales. As the current study illustrates, these can have a great impact on the design of novel mechanofluorochromic molecular systems, instrumentation techniques, and next-generation force sensors/quantification devices.

### 4. Experimental Section

*Macroscale Characterization:* Absorption spectra were recorded on a Cary 5000 spectrophotometer from Agilent Technologies. Emission spectra and quantum yields were measured on a Fluorolog-3-221 from Horiba Jobin Yvon. For quantum yield measurement of solid samples, an integrating sphere (Quanta- $\phi$ ) from Horiba Jobin Yvon using the method developed by de Melo and co-workers was employed.<sup>[55]</sup> In this set-up, film samples were fabricated directly on previously cleaned quartz substrate.

*Microscopy:* For wide-field imaging in Section 2.2, the microscopy set up involving a coupled AFM and optical microscope as previously described<sup>[30,32]</sup> was used. For force-fluorescence correlations, (Section 2.4) fluorescence recovery was calculated as the difference in emission intensity before and after stimulation. Error bars indicate the heterogeneity of emission signal taken over the stimulated area.

In both cases, AFM images were acquired with a JPK NanoWizard-3 instrument. The head of the AFM was installed on an inverted optical microscope (Nikon, Eclipse Ti-U). AFM topography was recorded in tapping mode under ambient conditions. Silicon cantilevers (Nanosensors, PPP-NCHR, tip height  $\approx 10 \mu\text{m}$ , tip radius curvature  $< 10 \text{ nm}$ , force constant  $\approx 40 \text{ N m}^{-1}$ , length =  $125 \mu\text{m}$ ) were used after calibration of their spring constant using a thermal noise procedure included in the JPK software. Image analysis was performed using the JPK analysis software. During stimulation, AFM tip was set to contact mode. A contact scan on an empty space was performed poststimulation to ensure that the tip did not pick-up the material (Figure S20, Supporting Information).

Wide-field imaging (Section 2.2): the sample was excited at 480 nm by a LED light source (Lumencor, Spectra X) and the signal was collected by an objective lens (Nikon 60X/0.95 ON Plan Apo  $\lambda$ ) separated from the incident excitation beam by a dichroic filter set (LF488/LP-B-000, Semrock) and sent to an EMCCD camera (Andor iXon Ultra 897).

Confocal and Hyperscan mode (Section 2.3): A typical experimental workflow involving confocal imaging, hyperspectral scans, and AFM tip stimulation is illustrated on Figure S9 (Supporting Information). First, a confocal image (labeled “Confocal 1a”) was taken to locate the sample of interest followed by a hyperspectral scan (Hyperscan 1). A second confocal image (Confocal 1b) was taken to ensure that the sample stayed in place and degradation was minimal. Then, AFM imaging with the tip in tapping and contact modes were performed. Then, another cycle of confocal imaging (Confocal 2a), hyperspectral scan (Hyperscan 2), and confocal imaging (Confocal 2b) was performed to interrogate differences in emission signal and spectral shape poststimulation.

Confocal mode images were collected by following system on the Nikon microscope (same objective) with Di02-R442 dichroic filter and BLP01-R458-25 emission filter (Semrock). The sample glass slide was moved with piezo actuators stage (P545-3C7, Physik Instrumente) pixel by pixel. For each pixel (integration time is 1 ms), a Laser diode (OBIS 445 nm LX 75 mW, Coherent) was turned on and the fluorescence signal was recorded with an APD (SPCM-AQRH-W5, Excelitas). For these experiments a fixed pinhole of 100  $\mu\text{m}$  diameter was used. A homemade software was realized with Labview in order to synchronize Laser diode, piezo stage and APD for each pixel. The 2D picture was then reconstructed with all the pixels recorded.

Hyperspectral scans were done with the same confocal set up. A flip mirror was used to send light to APD for confocal mode or CCD spectrograph for hyperspectral mode (Acton SP2356 with Spec-10 400Br/LN-eXcelon CCD detector, Princeton Instrument). The spectrograph slit was fixed to 200  $\mu\text{m}$  which represent a resolution of less than 5 nm. The integration time was 1 s for hyperspectral experiment. The same Labview software was used to record the 2D picture. All the spectra were recorded with WinSpec software (Princeton Instrument). Another Labview software for analysis was used to make the reconstruction of the 2D picture with the spectra recorded taking into account the information of pixel position.

Confocal 1b (prestimulation) and Confocal 2a (poststimulation) were compared to show the mechanofluorochromic response upon AFM contact scans. In some images, this caused an increase in emission so much that it was necessary to lower the laser power lest the detector gets saturated. To achieve meaningful comparisons, the emission signal on Confocal 1b was normalized to that of Confocal 2a.

## Supporting Information

Supporting Information is available from the Wiley Online Library or from the author.

## Acknowledgements

This work was supported by the European Research Council (ERC StG-715757 MECHANO-FLUO grant to C.A). The authors warmly acknowledge Dr. Régis Guillot and Dr. Oleksandr Pasko for assistance with crystal structure analyses and discussions. This work was granted access to the HPC resources of CINES under the allocation 2018-A0050810547 made by GENCI.

## Conflict of Interest

The authors declare no conflict of interest.

## Data Availability Statement

The data that support the findings of this study are available in the supplementary material of this article.

## Keywords

atomic force microscopy, confocal microscopy, mechanoluminescence, photoluminescence, stimuli-responsive materials

Received: November 23, 2021

Revised: January 27, 2022

Published online: February 26, 2022

- [1] M. U. Urban, *Stimuli-Responsive Materials: From Molecules to Nature Mimicking Materials Design*, The Royal Society of Chemistry, Cambridge, UK 2016.
- [2] H. Wang, X. Ji, Z. Li, F. Huang, *Adv. Mater.* **2017**, *29*, 1606117.
- [3] X. Li, Z. Li, Y.-W. Yang, *Adv. Mater.* **2018**, *30*, 1800177.
- [4] D. Wu, A. C. Sedgwick, T. Gunnlaugsson, E. U. Akkaya, J. Yoon, T. D. James, *Chem. Soc. Rev.* **2017**, *46*, 7105.
- [5] B. Valeur, I. Leray, *Coord. Chem. Rev.* **2000**, *205*, 3.
- [6] Y. Sagara, M. Karman, E. Verde-Sesto, K. Matsuo, Y. Kim, N. Tamaoki, C. Weder, *J. Am. Chem. Soc.* **2018**, *140*, 1584.
- [7] M. Irie, T. Fukaminato, T. Sasaki, N. Tamai, T. Kawai, *Nature* **2002**, *420*, 759.
- [8] L. Hou, X. Zhang, G. F. Cotella, G. Carnicella, M. Herder, B. M. Schmidt, M. Pätzelt, S. Hecht, F. Cacialli, P. Samori, *Nat. Nanotechnol.* **2019**, *14*, 347.
- [9] M. El Gemayel, K. Börjesson, M. Herder, D. T. Duong, J. A. Hutchison, C. Ruzié, G. Scheicher, A. Salles, Y. Geerts, S. Hecht, E. Orgiu, P. Samori, *Nat. Commun.* **2015**, *6*, 6330.
- [10] M. Irie, T. Fukaminato, K. Matsuda, S. Kobatake, *Chem. Rev.* **2014**, *114*, 12174.
- [11] J. P. D. C. Calupitan, O. Galangau, T. Nakashima, T. Kawai, G. Rapenne, *ChemPlusChem* **2019**, *84*, 564.
- [12] B. Yoon, J. Lee, I. S. Park, S. Jeon, J. Lee, J. M. Kim, *J. Mater. Chem. C* **2013**, 2388.
- [13] X. Liu, W. J. Padilla, *Adv. Mater.* **2016**, *28*, 871.
- [14] M. W. Khalid, C. Whitehouse, R. Ahmed, M. U. Hassan, H. Butt, *Adv. Opt. Mater.* **2019**, *7*, 1801013.
- [15] D. Kitagawa, S. Kobatake, *Chem. Rec.* **2016**, *16*, 2005.
- [16] Q. Li, H. Zhu, F. Huang, *J. Am. Chem. Soc.* **2019**, *141*, 13290.
- [17] N. Mejer, P. K. Iyer, *Angew. Chem., Int. Ed.* **2018**, *57*, 8488.
- [18] O. S. Wenger, *Chem. Rev.* **2013**, *113*, 3686.
- [19] S. Mukherjee, P. Thilagar, *Angew. Chem., Int. Ed.* **2019**, *58*, 7922.
- [20] Y. Sagara, S. Yamane, M. Mitani, C. Weder, T. Kato, *Adv. Mater.* **2016**, *28*, 1073.
- [21] M. Luo, X. Zhou, in *Mechanochromic Fluorescent Materials: Phenomena, Materials, Applications* (Eds.: J. Xu, Z. Chi), Royal Society of Chemistry, Cambridge **2014**, pp. 7.
- [22] P. Gayathri, M. Pannippara, A. G. Al-Sehemi, P. P. Anthony, *New J. Chem.* **2020**, *44*, 8680.
- [23] Y. Jiang, D. Gindre, M. Allain, P. Liu, C. Cabanetos, J. Roncali, *Adv. Mater.* **2015**, *27*, 4285.
- [24] D. Genovese, A. Aliprandi, E. A. Prasetyanto, M. Mauro, M. Hirtz, H. Fuchs, Y. Fujita, H. Uji-I, S. Lebedkin, M. Kappes, L. de Cola, *Adv. Funct. Mater.* **2016**, *26*, 5271.
- [25] Z. Song, R. Liu, Y. Li, H. Shi, J. Hu, X. Cai, H. Zhu, *J. Mater. Chem. C* **2016**, *4*, 2553.
- [26] D. Li, G. Li, J. Xie, D. Zhu, Z. n Su, M. R. Bryce, *J. Mater. Chem. C* **2019**, *7*, 10876.
- [27] Y. Wang, T. Yang, X. Liu, G. Li, W. Che, D. Zhu, Z. Su, *J. Mater. Chem. C* **2018**, *6*, 12217.
- [28] Y. Dong, J. Zhang, A. Li, J. Gong, B. He, S. Xu, J. Yin, S. H. Liu, B. Z. Tang, *J. Mater. Chem. C* **2020**, *8*, 894.
- [29] C. Grashoff, B. D. Hoffman, M. D. Brenner, R. Zhou, M. Parsons, M. T. Yang, M. A. McLean, S. G. Sligar, C. S. Chen, T. Ha, M. A. Schwartz, *Nature* **2010**, *463*, 263.
- [30] L. Polacchi, A. Brosseau, R. Métivier, C. Allain, *Chem. Commun.* **2019**, *55*, 14566.
- [31] S. Stöttinger, G. Hinze, G. Diezemann, I. Oesterling, K. Müllen, T. Basché, *Nat. Nanotechnol.* **2014**, *9*, 182.
- [32] M. Louis, C. P. Garcia, A. Brosseau, C. Allain, R. Métivier, *J. Phys. Chem. Lett.* **2019**, *10*, 4758.
- [33] T. Suhina, B. Weber, C. E. Carpentier, K. Lorincz, P. Schall, D. Bonn, A. M. Brouwer, *Angew. Chem., Int. Ed.* **2015**, *54*, 3688.
- [34] L. Polacchi, A. Brosseau, R. Guillot, R. Métivier, C. Allain, *Phys. Chem. Chem. Phys.* **2021**, *23*, 25188.

- [35] L. Juhasz, R. D. Ortuso, K. Sugihara, *Nano Lett.* **2021**, *21*, 543.
- [36] M. Yamashita, S. Nagai, S. Ito, T. Tachikawa, *J. Phys. Chem. Lett.* **2021**, *12*, 7826.
- [37] J. P. Calupitan, A. Poirot, J. Wang, B. Delavaux-Nicot, M. Wolff, M. Jaworska, R. Metivier, E. Benoist, C. Allain, S. Fery-Forgues, *Chem. - Eur. J.* **2021**, *27*, 4191.
- [38] P. S. Hariharan, D. Moon, S. P. Anthony, *J. Mater. Chem. C* **2015**, *3*, 8381.
- [39] Z. Wang, P. Gu, G. Liu, H. Yao, Y. Wu, Y. Li, G. Rakesh, J. Zhu, H. Fu, Q. Zhang, *Chem. Commun.* **2017**, *53*, 7772.
- [40] Y. Hirai, A. Wrona-Piotrowicz, J. Zakrzewski, A. Brosseau, R. Guillot, R. Métivier, C. Allain, *Photochem. Photobiol. Sci.* **2020**, *19*, 229.
- [41] D. Tu, P. Leong, Z. Li, R. Hu, C. Shi, K. Y. Zhang, H. Yan, Q. Zhao, *Chem. Commun.* **2016**, *52*, 12494.
- [42] L. Bu, M. Sun, D. Zhang, W. Liu, Y. Wang, M. Zhen, Z. Xue, W. Yang, *J. Mater. Chem. C* **2013**, 2028.
- [43] Y. Lin, G. Chen, L. Zhao, W. Z. Yuan, Y. Zhang, B. Z. Tang, *J. Mater. Chem. C* **2015**, *3*, 112.
- [44] F. Zhao, C. Fan, Z. Chen, G. Liu, S. Pu, *RSC Adv.* **2017**, *7*, 43845.
- [45] S. Ito, T. Taguchi, T. Yamada, T. Ubukata, Y. Yamaguchi, M. Asami, *RSC Adv.* **2017**, *7*, 16953.
- [46] K. Mizuguchi, H. Kageyama, H. Nakano, *Mater. Lett.* **2011**, *65*, 2658.
- [47] T. Butler, W. A. Morris, J. Samonina-Kosicka, C. L. Fraser, *ACS Appl. Mater. Interfaces* **2016**, *8*, 1242.
- [48] H. Wu, C. Hang, X. Li, L. Yin, M. Zhu, J. Zhang, Y. Zhou, H. Ågren, Q. Zhang, L. Zhu, *Chem. Commun.* **2017**, *53*, 2651.
- [49] C. Carayon, A. Ghodbane, N. Leygue, J. Wang, N. Saffron-Merceron, R. Brown, S. Fery-Forgues, *ChemPhotoChem* **2019**, *3*, 545.
- [50] P. Josse, M. Allain, J. P. Calupitan, Y. Jiang, C. Cabanetos, J. Roncali, *Adv. Opt. Mater.* **2020**, *8*, 2000420.
- [51] A. Liess, A. Lv, A. Arjona-Esteban, D. Bialas, A. M. Krause, V. Stepanenko, M. Stolte, F. Würthner, *Nano Lett.* **2017**, *17*, 1719.
- [52] J. Wang, A. Poirot, B. Delavaux-Nicot, M. Wolff, S. Mallet-Ladeira, J. P. Calupitan, C. Allain, E. Benoist, S. Fery-Forgues, *Dalton Trans.* **2019**, *48*, 15906.
- [53] R. D. Ortuso, K. Sugihara, *J. Phys. Chem. C* **2018**, *122*, 11464.
- [54] A. Patra, S. P. Anthony, T. P. Radhakrishnan, *Adv. Funct. Mater.* **2007**, *17*, 2077.
- [55] J. C. de Mello, H. F. Wittman, R. H. Friend, *Adv. Mater.* **1997**, *9*, 230.